TiO$_2$ flakes as anode materials for Li-ion-batteries

Ming-Che Yang[a], Yang-Yao Lee[a,b], Bo Xu[c], Kevin Powers[b], Ying Shirley Meng[a,c,*]

[a] Department of Materials Science and Engineering, University of Florida, Gainesville, FL 32611, USA
[b] Particle Engineering Research Center, University of Florida, Gainesville, FL 32611, USA
[c] Department of NanoEngineering, University of California San Diego, La Jolla, CA 92093-0448, USA

ARTICLE INFO

ABSTRACT

Anatase titanium dioxide is a promising negative electrode material for Li-ion batteries. However, the low intrinsic electrical conductivity and poor cycling performance have limited its application. In this work, titanium dioxide flakes have been synthesized through a simple spreading method that is easily scalable. The calcined titanium dioxide flakes exhibit larger reversible charge/discharge capacity, better rate capability and excellent cycling stability compared to anatase titanium dioxide nanoparticles. The larger surface area of the flakes leads to a larger electrode/electrolyte contact area, shorter solid state path lengths for both Li-ion and electron transport, which results in the better rate capability. The cycling performance was significantly improved by the porous structure of the calcined titanium dioxide flakes. Strategies for improving the volumetric energy density of the flakes are also discussed.

© 2012 Elsevier B.V. All rights reserved.

1. Introduction

Anatase titanium dioxide is a promising negative electrode material for Li-ion batteries due to its safety against overcharging and stable voltage plateau at 1.78 V, which made it possible to be paired with high voltage (5 V) cathode materials such as LiNi$_{0.5}$Mn$_{1.5}$O$_4$ [1–3]. However, the low electrical conductivity, poor rate capability and poor cycling performance caused by the structural changes during the lithiation process have limited its applications.

Several different methods have been developed to address these issues. Wagemaker [4] investigated the dependence of insertion reactions to titanium dioxide particle sizes and revealed progressively increasing Li capacity and Li-ion solubility with decreasing particle sizes. This result was also confirmed by other groups [5–7]. Besides the nanosized particle samples, various of titanium dioxide with different phases had been fabricated by several groups. Bruce et al. [2,8–10] synthesized TiO$_2$-B nanowires by a hydrothermal reaction to increase the discharge capacity and improve the cycling performance. Hu et al. [11] proved that difference occurs in the Li-insertion behavior between micrometer and nanosized rutile TiO$_2$. Up to 0.8 mol of Li can be inserted into nanometer-sized rutile TiO$_2$ at room temperature, while only 0.1–0.25 mol of Li can be inserted into micrometer-sized rutile TiO$_2$. Nevertheless, the dif-

ficulty of fabricating the nano-sized rutile TiO$_2$ limits its validity. Moreover, various of nanostructures had also been fabricated, such as nanofibers [12], nanorods [13], nanotubes [14–16], mesoporous films [17,18], laminar TiO$_2$ [19] and hollow ribbon nano-network structures [20], which were characterized with different surface areas, porosities and shapes that can significantly enhance the kinetics and improve electrochemical properties [21–23]. Using these low dimensional nanostructures as the building blocks, new electron and ion transportation pathways can be established as a new strategy.

Although many different synthesis methods were developed, these processes are complex, time-consuming and difficult to be applied in large-scale synthesis. To reduce the complexity and the price of precursors of conventional synthesis process, such as non-ionic surfactant template method and sol–gel method [24,25], a simple spreading method was used in this paper to make novel TiO$_2$ flakes. In particular, the porous TiO$_2$ flakes exhibit larger reversible charge/discharge capacity, better rate capability and excellent cycling stability compared to anatase titanium dioxide nano-particles. The thermal reaction process of the flakes was investigated by thermogravimentic differential thermal analysis (TG/DTA). The phase, structure, morphology and size distribution were examined by X-ray diffraction (XRD), high-resolution transmission electron microscopy (TEM) and scanning electron microscopy (SEM). The surface area and pore sizes were monitored by physisorption measurements. The relations between crystal structure, surface area, pore volume and electrochemical properties of anatase TiO$_2$ flakes were examined. The nano-sized grains of TiO$_2$ flakes, the pore volume and the surface area are all key factors contributing to the enhanced electrochemical properties.

* Corresponding author at: Department of NanoEngineering, University of California San Diego, La Jolla, CA 92093-0448, USA. Tel.: +1 8588224247; fax: +1 8585349553.
E-mail address: shirleymeng@ucsd.edu (Y.S. Meng).

2. Experimental methods

2.1. Sample preparation

Titanium dioxide flakes (F-TiO$_2$) were fabricated by spreading a mixture of stearic acid (Fisher, 99%), low surface tension hydrocarbon (Fisher, 97%) and titanium *n*-butoxide (Aldrich, 97%) on the surface of high purity water (Barnstead Nanopure Infinity, 18 M(cm^{-1}). Stearic acid and the hydrocarbon were used to decrease the viscosity of titanium dioxide precursor and enhance the spreadability of the mixture. Typically, a ratio of 1:8 of titanium *n*-butoxide to hydrocarbon was used to produce titanium dioxide flakes with thickness about 40 nm. The resulting slurry was washed with Nanopure water and then centrifuged (Begman BH-2) at 3000 rpm for 15 min to concentrate the slurry. The precursor was then suspended in isopropanol and centrifuged to remove further impurities. This process was repeated for a total of five times. After solvent exchanging with isopropanol alcohol ((CH$_3$)$_2$CHOH), the flakes were dried by a supercritical fluid drying process [26]. The 400 °C heat treatments were applied using a programmable electric furnace with a desired heating rate of 1 °C min^{-1} for 2 h in the air to make the calcined flakes (CF-TiO$_2$).

2.2. Characterization

Differential thermal analysis–thermogravimetry TG/DTA measurements were carried out by a Pyris diamond TG/DTA at a heating rate of 20 °C min^{-1} with a 200 ml min^{-1} flow rate in N$_2$ to understand the thermal reaction process such as weight loss and phase formation temperature of the F-TiO$_2$. X-ray powder diffractions of all samples were taken using XRD Philips APD 3720 using a Cu Kalpha radiation source operated at 45 kV and 20 mA. The scan speed was 3 s/step with a step size of 0.02° in two theta. A Quantachrome NOVA 1200 was used to perform the physisorption measurements. Prior to gas adsorption, the samples are degassed and dried in a vacuum oven at elevated temperatures. Surface area, total pore volume, average pore radius, and BJH pore size distribution can be determined based on the adsorption or desorption isotherm. Field emission scanning electron microscopy (FEG-SEM, JEOL JSM-6335F) was carried out to investigate the particle sizes and morphologies. Images were collected with an accelerating voltage of 10 kV. The sizes of the flakes distribution were examined by Particle Size Analyzer Coulter LS13320. The flakes were suspended on a copper grid with lacey carbon and investigated by using a field emission gun JEOL 2010F high-resolution transmission electron microscopy (TEM) with an accelerating voltage of 200 kV. The band gap of the titania samples were estimated by UV–visible diffuse reflectance spectroscopy using a Perkin-Elmer Lambda 800 UV/Vis spectrometer in the wavelength range of 250–500 nm.

2.3. Electrochemical testing

The electrochemical properties of anatase TiO$_2$ particles (Fisher, 99.9%, average size 50 nm diameter seen by SEM), F-TiO$_2$ and CF-TiO$_2$ electrodes were measured using 2016 coin cells consisting of metallic lithium as an anode and an electrolyte comprised of 1 M LiPF$_6$ in a 1:1 volume fraction of ethylene carbonate (EC)/dimethyl carbonate (DMC). A Celgard model C480 separator (Celgard Inc., USA) was used. Anode films were prepared from slurries of TiO$_2$ nanomaterials with 20% polyvinylidene fluoride (PVDF) and 20% acetylene carbon black dissolved in N-methyl-2-pyrrolidinone (NMP). The mixtures were cast onto Al foil using a doctor blade and dried at 100 °C overnight. The cast film was cut into cathode discs containing 2–3 mg of active materials before storing them in argon filled glove box (H$_2$O level < 1.6 ppm). The coin-cells were assembled in the glove box and tested using an Arbin BT2000 instrument
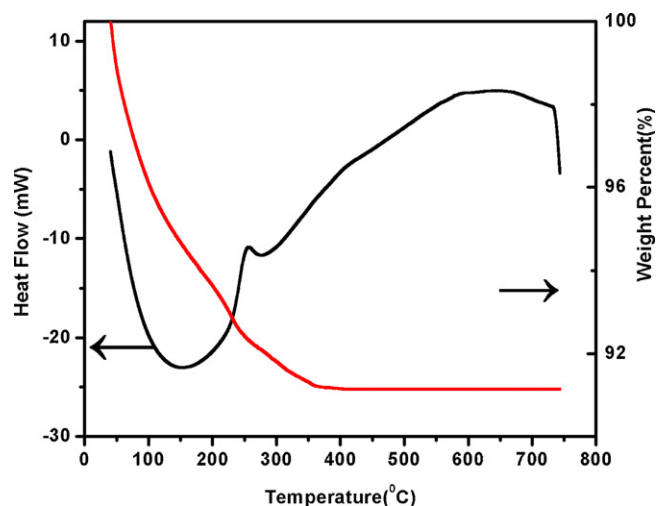

Fig. 1. TG/DTA measurements of F-TiO$_2$.

in galvanostatic mode. The tests were conducted between 3.5 V and 1 V at a constant current rate of C/20, C/10, C/5, C/2C and 2C. For cycling performance, tests were conducted with a voltage window between 3.5 V and 1 V at a constant current rate of C/20.

3. Results and discussion

3.1. Materials characterization

Fig. 1 shows the TG–DTA curves for the F-TiO$_2$ with a weight loss of about 9% at the temperature range from room temperature to 400 °C, which was resulted from either the desorption of water and isopropanol or the decomposition of organic compounds. According to the DTA data, a broad endothermic peak around 150 °C is present and is attributed to the loss of water and the organic residues absorbed at the surface of the flakes. There is a relatively small exothermic peak at 255 °C that was contributed to the decomposition of titanium *n*-butoxide in the pristine F-TiO$_2$. The observed exothermic peaks at 400 °C and 600 °C were due to the phase transformations from amorphous to crystalline anatase phase, and from anatase phase to the rutile phase, respectively.

Crystalline structural changes of the F-TiO$_2$, CF-TiO$_2$ and particles (Fisher, average 50 nm diameter) were monitored by XRD. As shown in Fig. 2, the F-TiO$_2$ shows broadened and weak Bragg peaks,
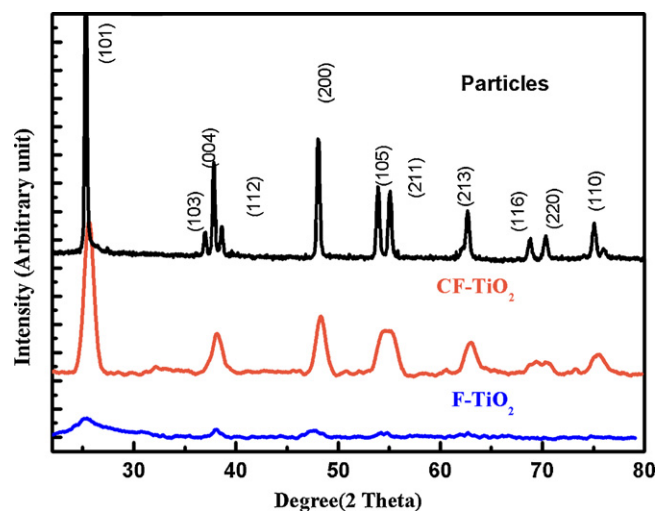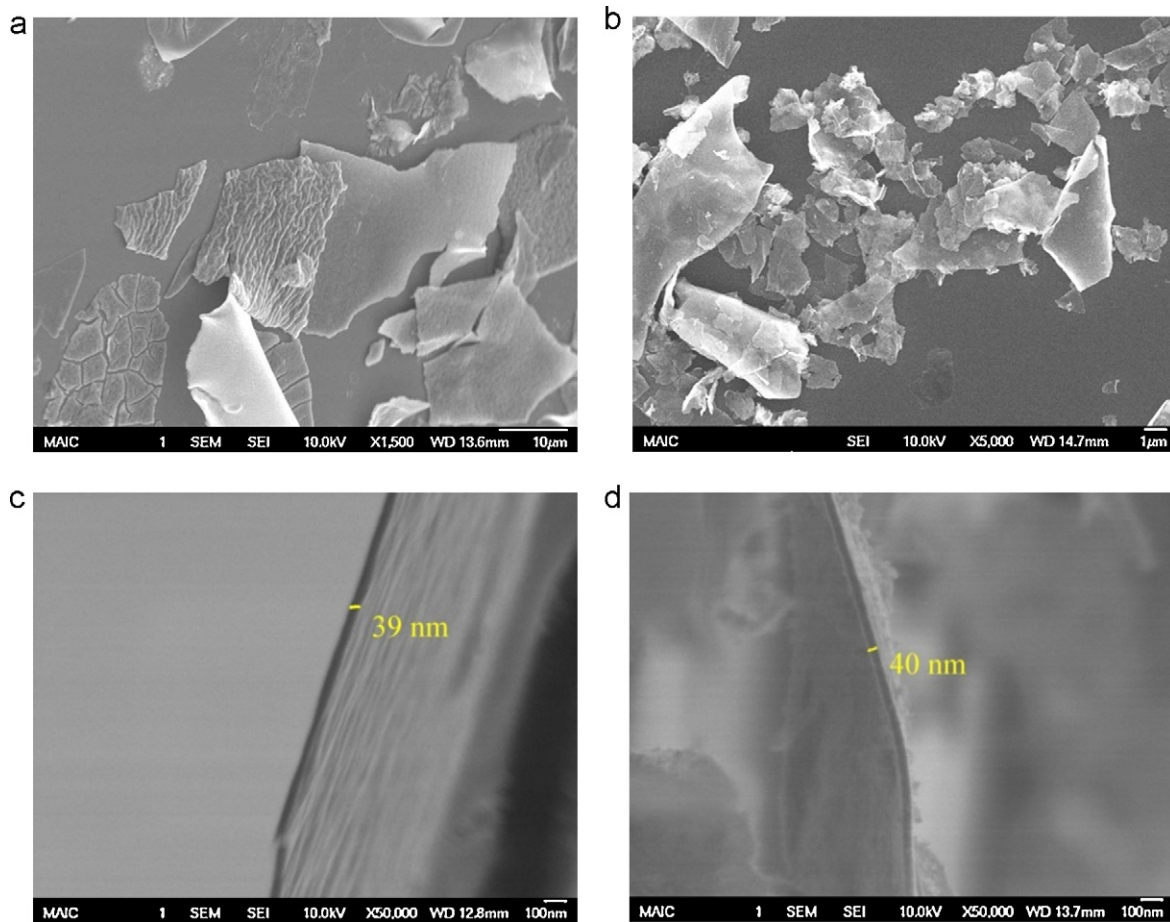

Fig. 2. X-ray diffraction patterns of TiO$_2$ samples.

Fig. 3. FESEM images of TiO_2 samples. (a) $F-TiO_2$; (b) $CF-TiO_2$; (c) edge view of $F-TiO_2$ and (d) edge view of $CF-TiO_2$.

which indicate that the flakes are partially amorphous with presence of the crystalline anatase phase. After a 2 h heat treatment at 400 °C, the expected phase transformation from the amorphous to crystalline anatase titanium dioxide was confirmed by the seven distinct characteristic diffraction peaks. The XRD results were identical to the TG–DTA results confirming that the heat treated flakes were converted to a pure crystalline anatase phase. There is no indication of any rutile phase by XRD. Compared to the powder sample, the diffraction peaks of the flakes are broadening and overlap with each other due to the smaller grain size. The average crystal grain size can be calculated by the Scherrer equation:

$$d = \frac{k\lambda}{B\cos\theta_B}$$

where d is the calculated grain size, λ is the wavelength of X-ray (Cu Kα 1.54 Å), B is the full-width at half-maximum intensity, and θ_B is the Bragg diffraction angle. The grain sizes of $F-TiO_2$ and $CF-TiO_2$ are determined to be 4 nm and 9 nm, respectively.

SEM was performed to examine the particle size and morphologies of TiO_2 flakes. The surface morphology of $F-TiO_2$, and the thickness are shown in Fig. 3(a–c). The lateral dimension of the $F-TiO_2$ was found to be in the order of 20–30 μm (Fig. 3(a)), and the thickness of these flakes is approximately 40 nm (Fig. 3(c)). The apparent thin-sheet morphology was explored and the aspect ratio of the lateral dimension to thickness ranged from 250:1 to 500:1. The flakes were further treated by calcination at 400 °C in air for 2 h. Aggregation was not apparent when comparing the $CF-TiO_2$ (Fig. 3(b)) with the $F-TiO_2$ (Fig. 3(a)). Moreover, the thickness of the $CF-TiO_2$ did not change by the heat treatment, as shown in Fig. 3(d).

A comparison of the measured particle size distribution of $F-TiO_2$ and $CF-TiO_2$ by laser diffraction is shown in Fig. 4. With the differential volume distribution of flakes that moved in turbulence and passed the laser beam, the maximum diameter was measured through the average random orientation of the flakes. The lateral dimension of flakes was estimated by dispersing both flakes in deionized water with liquid modules and were fairly close to the
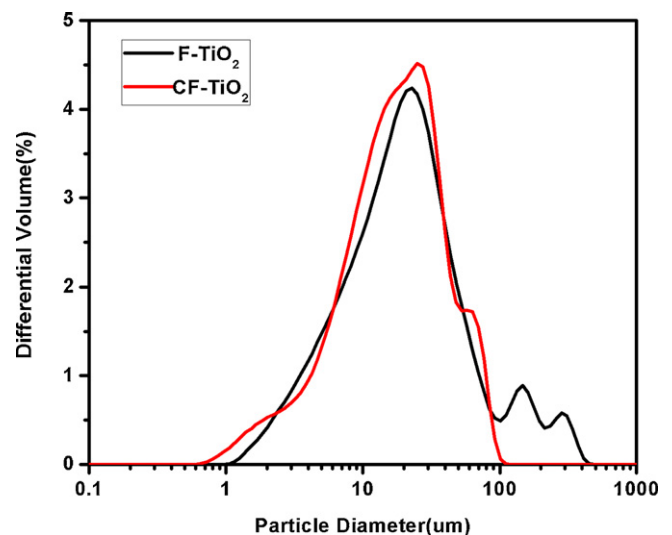

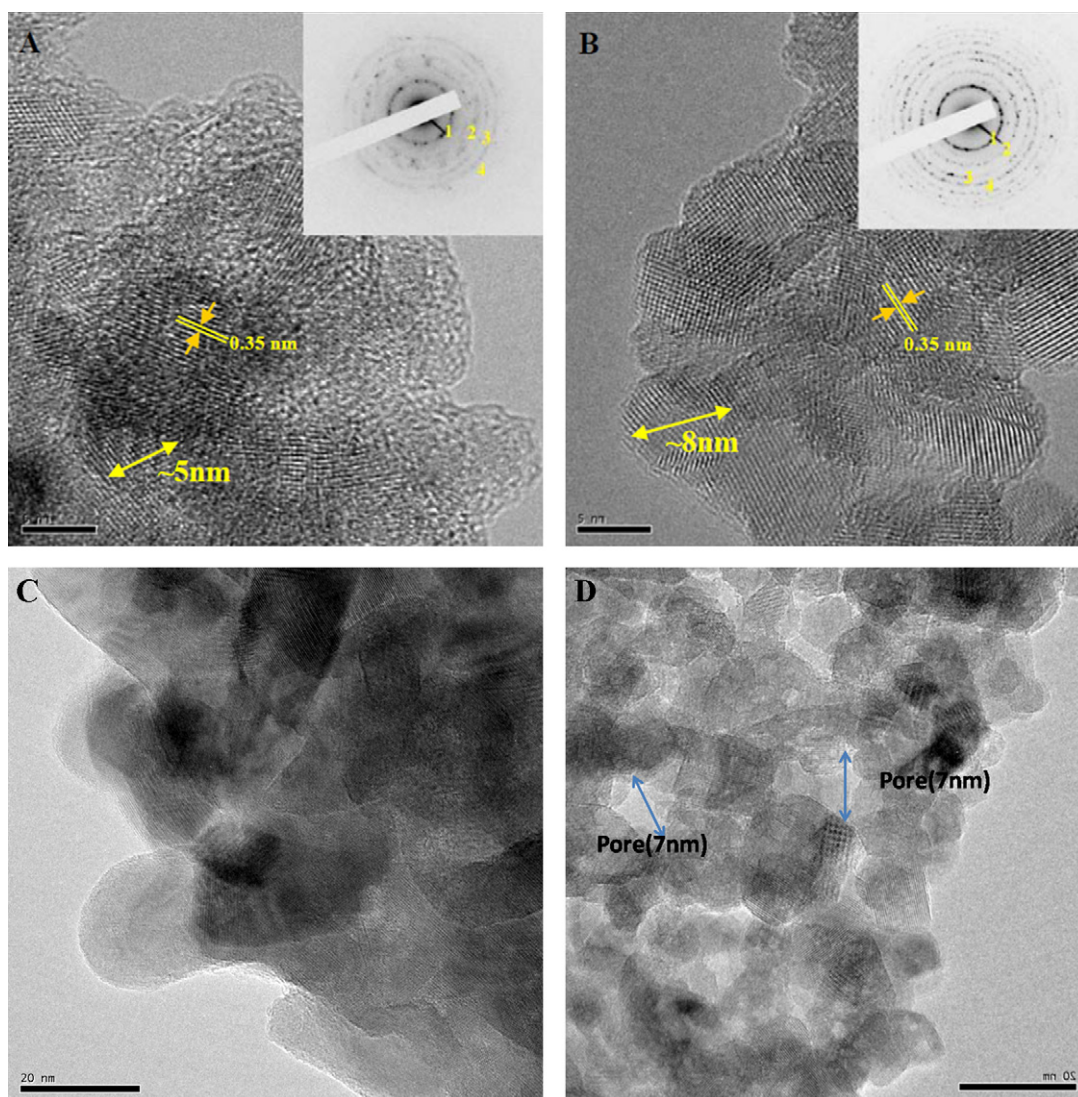**Fig. 4.** Particle size distribution for $F-TiO_2$ and $CF-TiO_2$ by laser diffraction.

Fig. 5. HR-TEM images of TiO$_2$ samples (the SAD pattern as inset). (a) F-TiO$_2$ and (b) CF-TiO$_2$. The diffraction rings are indexed as (1) (1 0 1); (2) (0 0 4); (3) (2 0 0) and (4) (1 0 5) for anatase. (c) F-TiO$_2$ and (d) CF-TiO$_2$.

results taken from the SEM images (Fig. 3(a and b)). The D10, D50, D90, mean and standard deviation values for the particle size distributions are shown in Table 1. F-TiO$_2$ has a broad size distribution spanning from 1 to 100 μm while the D50 for the F-TiO$_2$ and CF-TiO$_2$ are of 39.1 and 23.5 μm, respectively. It is evident that some larger flakes broke or cracked during dehydration and crystallization.

The crystalline structure of the flakes was further investigated under HR-TEM. The images show that the F-TiO$_2$, and CF-TiO$_2$ were comprised of crystalline platelets of about 5 and 8 nm in diameter (Fig. 5(a and b)), respectively. The interference lattice fringes can be seen in the TEM images and has a separation distance of 0.35 nm, corresponding to the interplanar spacing of the (1 0 1) planes for anatase [27]. Random orientation of individual grains over both F-TiO$_2$ and CF-TiO$_2$ samples is observed from the

concentric diffraction rings in the selected area diffraction mode and consistent with the anatase (1 0 1), (0 0 4), (2 0 0), (1 0 5) diffraction planes (the insets in Fig. 5(a and b)). On a closer inspection, an amorphous layer can be seen surrounding the smaller crystallites in the F-TiO$_2$ sample. An overall dense structure was seen in the F-TiO$_2$, as shown in Fig. 5(c). After the calcination process, pores with an average size of 7 nm were developed, as shown in Fig. 5(d), due to local rearrangement caused by the growth of crystal grains and by removing the residual solvent. Consequently, it is considered that the CF-TiO$_2$ are polycrystalline consisting of fine nano-grains and nano-size pores.

Surface area and porosity measurements were performed to quantify the changes of the titanium dioxide flakes after the calcination treatments. This was measured using the nitrogen absorption isotherms in conjunction with the Brunauer–Emmett–Teller (BET) model. It is desirable for anode materials to have higher specific surface areas that are able to increase the electrode and electrolyte contact area. Compared to commercial TiO$_2$ nanoparticles, the surface area of F-TiO$_2$ was 15 times higher (in Table 2), while the surface area of the CF-TiO$_2$ was still 7.5 times higher than that of TiO$_2$ nanoparticles. The BET measurements also show that the pore size of the calcined flakes is about 7.2 nm, which is consistent with the TEM observation.

Table 1
Particle diameter statistics for F-TiO$_2$ and CF-TiO$_2$.

	D10 (μm)	D50 (μm)	D90 (μm)	Median (μm)	Standard deviation (μm)
F-TiO$_2$	5.2	39.1	81.6	20.8	58.9
CF-TiO$_2$	5.1	23.5	50.1	18.4	18.8

Table 2
Surface area and pore size of TiO_2 particles, $F-TiO_2$ and $CF-TiO_2$.

	Specific surface area ($m^2 g^{-1}$)	Specific pore volume ($cm^3 g^{-1}$)	Average pore diameter (nm)
$F-TiO_2$	309		
$CF-TiO_2$	151	0.511	7.2
Particles	20		

Fig. 6 shows the typical UV–visible diffuse reflectance spectra in the wavelength range of 250–500 nm for the $F-TiO_2$ and $CF-TiO_2$. The sharp decrease in the diffuse reflectance in the UV region is attributed to the fundamental light absorption of the TiO_2 flakes. The spectral profile for $CF-TiO_2$ was apparently blue-shifted compared with that of the $F-TiO_2$. The general relation between the absorption coefficient and the band gap energy is given by the equation:

$$(\alpha h\nu)^m = h\nu - Eg$$

where m is an index depending on the nature of the electron transitions, α is the absorption coefficient, h is the Planck constant, ν is the frequency of electromagnetic radiation, and Eg is band gap energy of the semiconductor. The estimated band gap energies of the as-prepared and calcined flakes are 3.25 and 3.33 eV, respectively. Both values are higher than the band gap energies of nanoparticles (3.2 eV). The increase of the band gap is most likely due to the quantum confinement effect [27].

3.2. Electrochemical properties

3.2.1. Charge–discharge studies

The electrochemical properties of the TiO_2 powder, $F-TiO_2$ and $CF-TiO_2$ were investigated using lithium half-cells with a constant current $0.1\,mA\,cm^{-2}$. The first discharge/charge profiles between 3.5 and 1.0 V are shown in Fig. 7(a and b). As Fig. 7(a) shows, there is a plateau around 1.75 V for TiO_2 nanoparticles and $CF-TiO_2$ that corresponds to the occurrence of the two phase equilibrium of Lithium-poor ($Li_{0.01}TiO_2$) and Lithium-rich ($Li_{0.6}TiO_2$) domains [28]. However, there is no voltage plateau observed in the $F-TiO_2$. The amorphous phase of the $F-TiO_2$ seen by TEM and the smaller grain size [4] may be the contributing factors to the sloping voltage curve. The lithium intercalation/deintercalation reaction in this region can be written as:
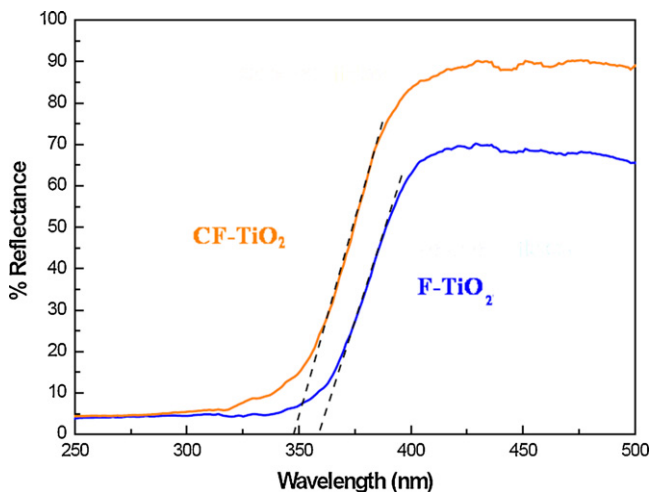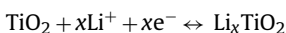
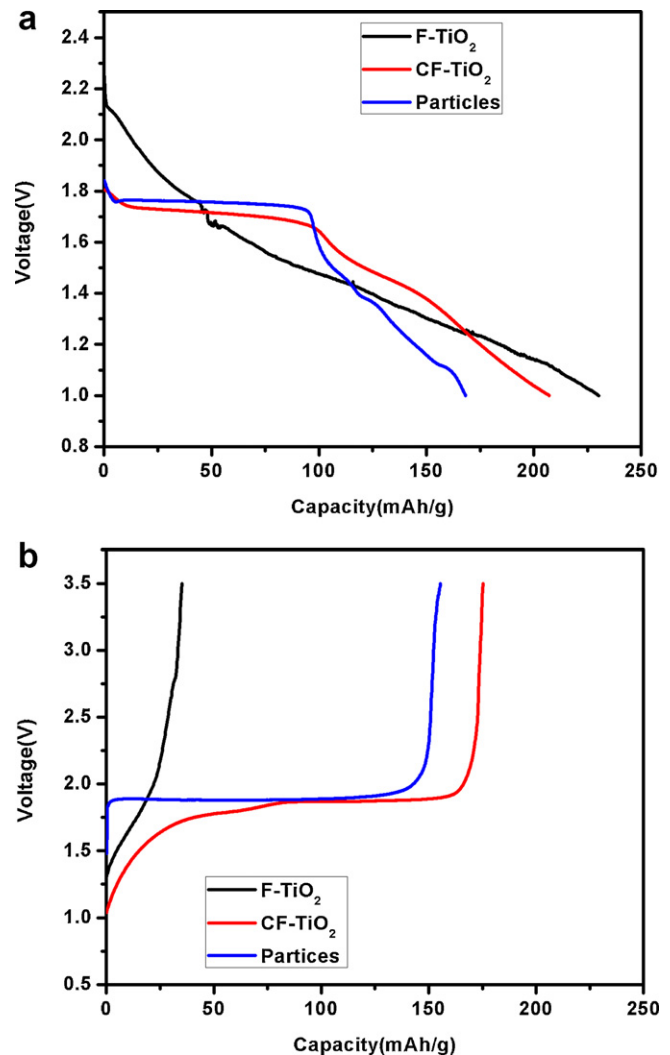$$TiO_2 + xLi^+ + xe^- \leftrightarrow Li_xTiO_2$$

Fig. 7. (a) First discharge curves of TiO_2 samples and (b) first charge curves of TiO_2 samples.

The amount of lithium insertion depends on the crystallinity, morphology as well as the microstructure. Generally, increasing the specific surface area or decreasing the particle size for anatase TiO_2 particles can increase the discharge capacity [5]. In our work, the flakes show a similar trend. The capacity, grain size and specific surface area for $F-TiO_2$, $CF-TiO_2$ and nanoparticles are ($238\,mA\,h\,g^{-1}$, 5 nm, $309\,m^2\,g^{-1}$), ($213\,mA\,h\,g^{-1}$, 8 nm, $151\,m^2\,g^{-1}$), and ($170\,mA\,h\,g^{-1}$, 50 nm, $20\,m^2\,g^{-1}$), respectively. Although the $F-TiO_2$ have the largest 1st cycle discharge capacity, the first cycle charge capacity is very small, as shown in Fig. 7(b). Apparently, the lithiation reaction was not reversible for the $F-TiO_2$. Although the surface area and the grain size are key factors to determine the electrochemical properties, the amorphous phase (Figs. 2 and 5(a)), residual organic precursors (Fig. 1) and denser microstructure (Fig. 5(c)) lead to the poor electrochemical performance. The supercritical drying process during the preparation of the $F-TiO_2$ can induce a partially crystallized anatase phase and keep the largest surface area, but the enhanced electrochemical performance can be achieved only after the 400 °C post-synthetic calcination process. For the anatase TiO_2 nanoparticles, the discharge/charge capacity is about $170\,mA\,h\,g^{-1}$, corresponding to $Li_{0.5}TiO_2$ that is identical to the conventional anatase TiO_2 materials. The $CF-TiO_2$ exhibit a 1st cycle discharge capacity exceeding $200\,mA\,h\,g^{-1}$ and subsequent discharge/charge capacities of $180\,mA\,h\,g^{-1}$. Interesting

Fig. 6. UV–visible diffuse reflectance spectra of $F-TiO_2$ and $CF-TiO_2$.
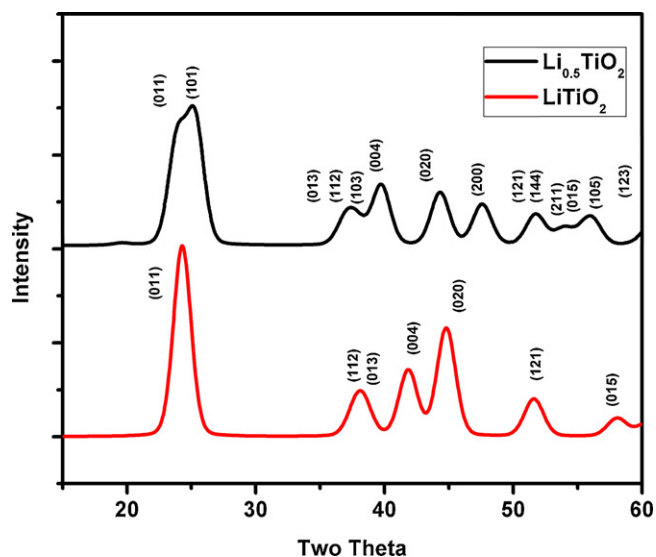
Fig. 8. The XRD patterns of $Li_{0.5}TiO_2$, $LiTiO_2$ simulated by Crystal Diffraction.

Fig. 9. Rate capability comparison of $CF\text{-}TiO_2$ and TiO_2 particles.

observations can be made through comparing the discharge and charge curves in Fig. 7: the length of the biphasic region (plateau region) corresponds to the number of lithium ions inserted into the bulk lattice [5]. Therefore, the capacity in the plateau region should decrease for smaller grain sizes, as observed by others [5]. Although the grain size of the $CF\text{-}TiO_2$ (8 nm) is much smaller than that of the nanopowders (50 nm), the capacity of the plateau region is similar to that of nanoparticles. Obviously, the $CF\text{-}TiO_2$ still keep some bulk characteristics. On the other hand, the capacity of the sloping region for $CF\text{-}TiO_2$ is larger than that in the TiO_2 nanoparticles, thus implies that Li ions are further inserted into the surface layer [6]. Upon the first charging, a sloping region can be clearly observed at the beginning of the charge as well. Wagemaker et al. have shown that anatase TiO_2 nanoparticles can completely convert to the Li_1TiO_2 phase if the particle size is smaller than 7 nm [4]. The grain size of the flakes is between 5 and 8 nm which suggests the new Li_1TiO_2 phase may form during the lithiation process and lead to a larger capacity compared to that of the nanoparticles (50 nm). In theory, the bulk $Li_{0.5}TiO_2$ and $LiTiO_2$ phase have distinct diffraction peaks and the extra peaks should be detected by the ex situ XRD. However, it is difficult to differentiate the overlapping peaks of nano-sized $Li_{0.5}TiO_2$ and $LiTiO_2$ because the serious peak broadening for the nano-sized materials. The XRD patterns of $Li_{0.5}TiO_2$ and $LiTiO_2$ were simulated using the Crystal Diffraction software with 5 nm particle size, shown in Fig. 8. The major peaks of $Li_{0.5}TiO_2$ and $LiTiO_2$ overlap significantly. In practice, the peak broadening from the laboratory instrument also has to be considered. Therefore, the Li_1TiO_2 phase cannot be identified clearly by conventional laboratory XRD. High-resolution neutron diffraction experiments are necessary to identify the detailed structural change. According to Wagemaker et al. [4], the neutron diffraction has identified the new $LiTiO_2$ phase in 7 nm TiO_2 nanoparticles.

3.2.2. Rate capability performance

To study the rate capability of TiO_2 nanomaterials, electrodes were made with similar loading of active materials in each cell (about 5 mg active material cm^{-2}). For each material, the cells were discharged to 1 V at constant rates (C/20) and charged to 3.5 V at various current rates (C/20, C/10, C/5, C/2, C and 2C). The measured 1st cycle charge capacities with different current densities were shown in Fig. 9. Clearly, $CF\text{-}TiO_2$ show better rate performances than TiO_2 nanoparticles. The charge capacity of the $CF\text{-}TiO_2$ tested at 2C still retains 48.44% of its capacity, compared to the capacity at
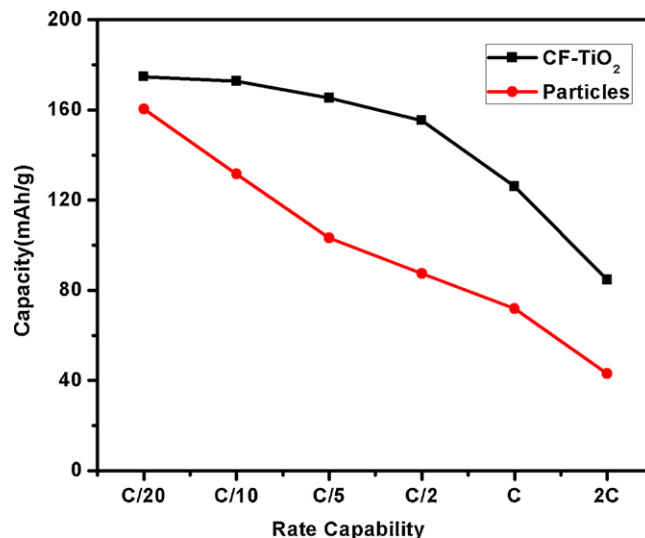
C/20. On the other hand, the charge capacity of TiO_2 nanoparticles tested at 2C decreased to 26.81%, compared to the capacity at C/20.

Nano size effects of electrochemical energy storage systems can be divided into two categories; [22] The first is the *true* size effects, which involve changes of actual materials, including the change of structure and phase stability, electronic band gap and intrinsic diffusivity, etc. The second is the *trivial* size effects, and the result of trivial size effect is largely relied on the surface-to-volume ratio, the shape and the pores of the nanomaterials.

TiO_2 is an intrinsically low electronic conductive material. The quantum confinement effects show that the band gap will increase for decreased particle size, confirmed in our UV–vis diffuse reflectance measurement. The band gap of nanoparticles, $F\text{-}TiO_2$ and $CF\text{-}TiO_2$ are 3.20 eV, 3.25 eV and 3.33 eV, respectively. This implies that the intrinsic electronic conductivity of the calcined TiO_2 flakes will decrease. Moreover, Wagemaker et al. [29,30] used static ^7Li NMR T2 relaxation measurements to probe the Li-ion mobility of micro and nanosize anatase TiO_2. The result shows that the lithium diffusion coefficient for nanomaterials is lower than that for the microsized materials. Nevertheless, our electrochemical data clearly show that the $CF\text{-}TiO_2$ have superior electrochemical properties.

For the flakes, the *trivial* size effects should be the key factors that contribute to the excellent rate capability. The specific surface area of the $CF\text{-}TiO_2$ is 7.5 times than the nanoparticles. The large surface area can lead to larger electrode/electrolyte contact area that can improve the ionic conductivity. At the same time, nanostructured materials can provide short path lengths for both Li-ion and electron transport, even though the nanomaterials have intrinsically lower electronic and ionic conductivity. Considering that the diffusion length is scaled with time by $l \propto t^2$, the Li diffusion time may be much lower for 8 nm grains in the $CF\text{-}TiO_2$. Moreover, the larger surface area of nanostructured electrodes can also greatly reduce the specific current density of the active materials. The low specific current density can effectively stabilize the electrode and keep a high capacity at higher charge/discharge rate [22].

3.2.3. Cycling performance

The variation of specific charge/discharge capacity with respect to the cycle number of $CF\text{-}TiO_2$ and TiO_2 nanoparticles at a constant current density (C/20) was shown in Fig. 10. TiO_2 nanoparticles show a fast fading with the increasing of cycle number, while there is virtually no fading for the $CF\text{-}TiO_2$. The $F\text{-}TiO_2$ have poor cycling performance due to the residual solvent or amorphous
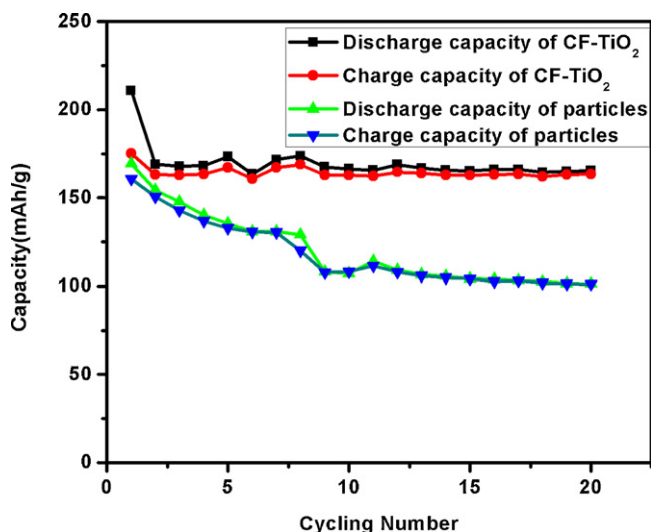
Fig. 10. The variation of specific discharge capacity with respect to the cycle number of CF-TiO$_2$ and particles.

phase present. CF-TiO$_2$ with nano-grains and nano-porous structure show an excellent cycling performance with high capacity. This makes it a promising anode material for Li-ion batteries. The porous structure is expected to supply the space to accommodate the volume change and preventing the undesired fractures or electronic disconnects of the electrode materials during the de-lithiation and lithiation process [12]. On the other hand, the lack of a two-phase boundary in nanosize < 8 nm TiO$_2$ is another possible reason for the improved cycling performance. Previous work by neutron diffraction shows two different lithiated mechanisms for the bulk and nano size anatase materials [4,31]. For bulk materials, the Li-titanate crystal phase will grow at the cost of the crystal anatase phase and induce extra strain during the lithiation process. However, for nano-sized particles (7 nm), either the anatase or the Li-titanate phase is detected during the lithiation process. This indicates that in extremely small particles, the two phases do not coexist in the same particle during the intercalation process. The unique nano-grains and nano-porous structure in CF-TiO$_2$ and the possible elimination of the phase boundary during lithiation lead to the excellent cycling performance.

The advantage of the porous structure can be tarnished by the low volumetric energy density. However in the case of flakes, it is possible to improve the volumetric energy density by packing the sheets of flakes aligned in a horizontal orientation. This methodology is in development and will be reported elsewhere.

4. Conclusion

In this work, titanium dioxide flakes were fabricated by a simple spreading method. This process is easy and scalability is high. The low surface tension hydrocarbon and titanium n-butoxide were used as the precursors and continuously added into the solution on the surface of flowing water. A supercritical drying process was performed to remove the residual water. The size of the synthesized flake is about 40 nm in the lateral dimension and was composed of 5 nm nanograins. After a 400 °C calcination process, the flakes transformed into a pure anatase phase that is free of any impurity. In this phase, the flakes are characterized to have 8 nm grains and the 7 nm pores. The crystal structure, surface area, pore size, electronic properties and electrochemical properties are compared for flakes and nanoparticles. The electrochemical and structural properties of the flakes are significantly influenced by subsequent heat treatment

process. The CF-TiO$_2$ exhibit larger reversible charge/discharge capacity, better rate capability and excellent cycling stability. The nano-sized grains (8 nm) may lead to the absence of two-phase in single particles during lithiation, improving the cycling performance significantly. A larger electrode/electrolyte contact area, short path lengths for both Li-ion and electron transport and lower specific current density of in the CF-TiO$_2$ lead to a much better rate capability.

References

[1] T. Ohzuku, S. Takeda, M. Iwanaga, Journal of Power Sources 81–82 (1999) 90–94.
[2] G. Armstrong, A. Armstrong, P. Bruce, P. Reale, B. Scrosati, Advanced Materials 18 (2006) 2597–2600.
[3] J.C. Arrebola, A. Caballero, M. Cruz, L. Hernán, J. Morales, E.R. Castellón, Advanced Functional Materials 16 (2006) 1904–1912.
[4] M. Wagemaker, W.J.H. Borghols, F.M. Mulder, Journal of the American Chemical Society 129 (2007) 4323–4327.
[5] C. Jiang, M. Wei, Z. Qi, T. Kudo, I. Honma, H. Zhou, Journal of Power Sources 166 (2007) 239–243.
[6] G. Sudant, E. Baudrin, D. Larcher, J.-M. Tarascon, Journal of Materials Chemistry 15 (2005) 1263–1269.
[7] V. Subramanian, A. Karki, K.I. Gnanasekar, F.P. Eddy, B. Rambabu, Journal of Power Sources 159 (2006) 186–192.
[8] A.R. Armstrong, G. Armstrong, J. Canales, P.G. Bruce, Journal of Power Sources 146 (2005) 501–506.
[9] A.R. Armstrong, G. Armstrong, J. Canales, P.G. Bruce, Angewandte Chemie International Edition 43 (2004) 2286–2288.
[10] A.R. Armstrong, G. Armstrong, J. Canales, R. García, P.G. Bruce, Advanced Materials 17 (2005) 862–865.
[11] Y.S. Hu, L. Kienle, Y.G. Guo, J. Maier, Advanced Materials 18 (2006) 1421–1426.
[12] M.V. Reddy, R. Jose, T.H. Teng, B.V.R. Chowdari, S. Ramakrishna, Electrochimica Acta 55 (2010) 3109–3117.
[13] S.-J. Bao, Q.-L. Bao, C.-M. Li, D. Zhi-Li, Electrochemistry Communications 9 (2007) 1233–1238.
[14] B.-L. He, B. Dong, H.-L. Li, Electrochemistry Communications 9 (2007) 425–430.
[15] J. Xu, C. Jia, B. Cao, W.F. Zhang, Electrochimica Acta 52 (2007) 8044–8047.
[16] G.F. Ortiz, I. Hanzu, T. Djenizian, P. Lavela, J.L. Tirado, P. Knauth, Chemistry of Materials 21 (2008) 63–67.
[17] L. Kavan, J. Rathousk, M. Grazel, V. Shklover, A. Zukal, Microporous and Mesoporous Materials 44–45 (2001) 653–659.
[18] P. Kubiak, J. Geserick, N. Hing, M. Wohlfahrt-Mehrens, Journal of Power Sources 175 (2008) 510–516.
[19] M.-C. Tsai, J.-C. Chang, H.-S. Sheu, H.-T. Chiu, C.-Y. Lee, Chemistry of Materials 21 (2009) 499–505.
[20] S.-W. Kim, T.H. Han, J. Kim, H. Gwon, H.-S. Moon, S.-W. Kang, S.O. Kim, K. Kang, ACS Nano 3 (2009) 1085–1090.
[21] P.G. Bruce, B. Scrosati, J.-M. Tarascon, Angewandte Chemie International Edition 47 (2008) 2930–2946.
[22] C. Jiang, E. Hosono, H. Zhou, Nano Today 1 (2006) 28–33.
[23] Y.-G. Guo, J.-S. Hu, L.-J. Wan, Advanced Materials 20 (2008) 2878–2887.
[24] A. Matsuda, T. Matoda, T. Kogure, K. Tadanaga, T. Minami, M. Tatsumisago, Chemistry of Materials 17 (2005) 749–757.
[25] T. Sasaki, S. Nakano, S. Yamauchi, M. Watanabe, Chemistry of Materials 9 (1997) 602–608.
[26] S. Tedeschi, N. Stevens, D. Cepeda, Y.-Y. Lee, K. Powers, M. Ranade, H. El-Shall, Powder Technology 191 (2009) 188–193.
[27] T. Sasaki, M. Watanabe, The Journal of Physical Chemistry B 101 (1997) 10159–10161.
[28] M. Wagemaker, A.P.M. Kentgens, F.M. Mulder, Nature 418 (2002) 397–399.
[29] M. Wagemaker, W.J.H. Borghols, E.R.H. van Eck, A.P.M. Kentgens, G.J. Kearley, F.M. Mulder, Chemistry – A European Journal 13 (2007) 2023–2028.
[30] M. Wagemaker, R. van de Krol, A.P.M. Kentgens, A.A. van Well, F.M. Mulder, Journal of the American Chemical Society 123 (2001) 11454–11461.
[31] W. Dreyer, J. Jamnik, C. Guhlke, R. Huth, J. Moskon, M. Gaberscek, Nature Materials 9 (2010) 448–453.